

Synthesis and analysis of structural, compositional, morphological, magnetic, electrical and surface charge properties of Zn-doped nickel ferrite nanoparticles

K. Anu, J. Hemalatha *

Advanced Materials Lab, Department of Physics, National Institute of Technology, Tiruchirappalli, 620015, Tamilnadu, India



ARTICLE INFO

Keywords:
Electrical conductivity
Magnetic
Surface charge
Zn-doped nickel ferrite
Nanoparticles
Morphology

ABSTRACT

Zn-doped nickel ferrite nanoparticles ($Zn_xNi_{(1-x)}Fe_2O_4$) were synthesized using the co-precipitation technique. The structural and compositional studies of the $Zn_xNi_{(1-x)}Fe_2O_4$ nanoparticles revealed their face-centred cubic spinel structure and an appropriate amount of Zn doping in nickel ferrite nanoparticles, respectively. The morphological analysis had been carried out to obtain the particle size of the synthesized nanoparticles. The magnetic studies revealed the superparamagnetic nature of the $Zn_xNi_{(1-x)}Fe_2O_4$ nanoparticles, and the maximum magnetization of 30 emu/g for the $Zn_{0.2}N_{0.8}Fe_2O_4$ sample. The M – H curves were fitted with the Langevin function to obtain the magnetic particle diameter of $Zn_xNi_{(1-x)}Fe_2O_4$ nanoparticles. The electrical conduction in $Zn_xNi_{(1-x)}Fe_2O_4$ nanoparticles was explained through the Verway hopping mechanism. The $Zn_{0.2}N_{0.8}Fe_2O_4$ nanoparticle exhibited a higher electrical conductivity of 42 μ S/cm and surface charge of $-29/7$ mV due to the enhanced hopping of Fe^{3+} ions in the octahedral sites. Owing to this nature, they were identified as the suitable candidates in the applications such as thermoelectrics, hyperthermia, magnetic coating and for the preparation of conducting ferrofluids.

1. Introduction

A group of materials called Spinel ferrites, MFe_2O_4 ($M^{2+} = Zn^{2+}$, Co^{2+} , Ni^{2+} , Mn^{2+} , Cd^{2+}) are significant due to their enhanced optical, magnetic, and electrical properties, which find various applications [1–7]. The unit cell of spinel ferrites has eight molecules and the face-centred cubic lattice is formed by the oxygen ions. The spinel structure has tetrahedral (64 voids) and octahedral site (32 voids) where the metal ions are located in crystallographically non-equivalent positions of octahedral [B] and tetrahedral (A) sites, which are formed by the oxygen ions through which the exchange interaction occurs in the spinel ferrite structure. For the spinel structure, both sublattice (A–A and B–B) and inter-sublattice (A–B) interactions are negative as the magnetic moments of the ions tend to orient antiparallelly to each other. As a result of the competition between these interactions, the inter-sublattice (A–B) interaction is dominant. Depending on the distribution of ions in the sublattice, the normal and inverse spinel structures are distinguished [Buschow, K., (2003)]. In the normal spinel structure, the divalent ions are in the tetrahedral positions; other ions are in octahedral positions, e.g. $ZnFe_2O_4$. The inverse spinel structure has divalent ions occupy the

octahedral sites and the trivalent ions are distributed in the tetrahedral and octahedral sites equally, e.g. $CoFe_2O_4$ and Fe_3O_4 . These materials are extensively analyzed due to their applications in microelectronic devices, magnetic data storage, gas sensing etc.,

Nickel ferrite ($NiFe_2O_4$) is one of the versatile and technologically important ferrite materials because of its typical superparamagnetic properties with moderate magnetization, moderate conductivity, high electrochemical stability, abundance in nature, etc., which finds applications in various fields [1–3]. The electrical, thermal, magnetic and optical properties of spinel ferrites depend on the various factors such as processing conditions, chemical composition and the quantity of dopants. These ferrites when doped with dia-magnetic atoms show a wide improvement in their physical properties [2–9]. The doping of divalent Zn^{2+} ions considerably affects the properties of spinel ferrites as reported [9–15]. Hence the main objective of the present work is to synthesize Zn-doped nickel ferrite nanoparticles, to analyze the effect of Zn doping on structural, magnetic, electrical and surface charge properties of the $NiFe_2O_4$ nanoparticles and to explore their usage in the practical applications.

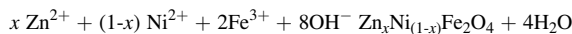
* Corresponding author.

E-mail address: hemalatha@nitt.edu (J. Hemalatha).

2. Synthesis and characterization of $Zn_xNi_{1-x}Fe_2O_4$ nanoparticles

The synthesis of $Zn_xNi_{1-x}Fe_2O_4$ nanoparticles were carried out through co-precipitation method, where the aqueous solutions of precursors viz zinc acetate ($Zn(O_2CCH_3)_2$), nickel nitrate ($Ni(NO_3)_2$), and ferric nitrate ($Fe(NO_3)_2$) taken in various stoichiometric ratios [Zn: Co: Fe = x: 1-x: 2] were used.

The $Zn_xNi_{1-x}Fe_2O_4$ nanoparticles were formed on the addition of precipitating agent NaOH to the precursor solution and the chemical reaction involved is as follows,



The obtained nanoparticles were cleaned several times with water to remove the impurities and dried at 150 °C for 4 h. The $Zn_xNi_{1-x}Fe_2O_4$ nanoparticles with the dopant concentration of x = 0, 0.1, 0.2, 0.3 and 0.4 were coded as PN0, PN1, PN2, PN3 and PN4, respectively (Fig. 1).

The XRD patterns obtained from X-ray diffractometer (model: Rigaku Ultima III) using $CuK_{\alpha 1}$ radiation ($\lambda = 0.15406$ nm) for 20 values ranging from 20° to 70° was used for the structural and phase compositional analysis of the magnetic nanoparticles. The morphological studies were done using the High Resolution Philips TECNAI F20 Transmission Electron Microscopy and ZEISS Sigma 300 Field Emission Scanning Electron Microscope to obtain the particle size of synthesized nanoparticles. The energy-dispersive X-ray spectroscope (EDS) [Vega 3 Tescan] was used for the quantitative analysis of the dopant in the synthesized nanoparticles. The vibrating sample magnetometer (Lakeshore Model 7410) was used to obtain the M – H plots of the synthesized nanoparticles. The synthesized nanoparticles are made into pellets of 0.5 mm diameter and by using copper electrode of area 3.2 mm² and the source measure unit (Keysight B2901 A) was used to obtain the I-V characteristics of those pellets. The nanoparticles were dispersed in water using a probe sonicator and the zeta potential measurements are carried out using Malvern Zeta sizer (ZS90).

3. Characterization of $Zn_xNi_{1-x}Fe_2O_4$ nanoparticles

3.1. Structural analysis of $Zn_xNi_{1-x}Fe_2O_4$ nanoparticles

The diffraction planes (220), (311), (400), (422), (511) and (440) of the $Zn_xNi_{1-x}Fe_2O_4$ nanoparticles as shown in Fig. 2 (a) matches well with the diffraction planes reported in the JCPDS card no. 22-1086 [3].

The XRD pattern clearly shows that the synthesized nanoparticles are of phase pure nature and they have face centred cubic inverse spinel structure. The doping of Zn in $NiFe_2O_4$ causes an expansion of crystal

lattice due to the larger ionic radius of Zn than Ni (0.72 Å) ion which results in the shift of diffraction planes towards the lower angle as shown in Fig. 2 (b). The lattice parameter (a_{expt}) is calculated using the following equation [16], where d and (hkl) are the interplanar distance and miller indices, respectively. According to the Vegard's law, unit cell parameters should vary linearly with composition for a continuous substitution of solid in which atoms or ions that substitutes each other. Fig. 2(c) shows the plot of lattice parameter of $Zn_xNi_{1-x}Fe_2O_4$ nanoparticles versus dopant concentration. An increasing trend of lattice parameter with respect to dopant concentration is observed as the lattice constant of Zn is higher than Ni, which shows that it obeys Vegard's law and the variation is attributed to the expansion of crystal lattice with respect to zinc doping.

The following equations are used to find the lattice parameter of the spinel ferrites theoretically [17–20], where R_0 is the ionic radius of oxygen (0.138 nm).

The synthesized $Zn_xNi_{1-x}Fe_2O_4$ nanoparticles exhibit an inverse spinel structure with the cationic distribution. The ionic radii (r_A and r_B) of (A) and [B] sites are calculated using the formulae, respectively, where $r(Zn^{2+})$, $r(Fe^{3+})$ and $r(Ni^{2+})$ are the ionic radii of Zn^{2+} (0.83 Å), Fe^{3+} (0.67 Å) and Ni^{2+} (0.74 Å), respectively and $C_{A(Zn)}$, are the concentrations of Zn^{2+} and Fe^{3+} ions on (A) sites and Ni^{2+} and Fe^{3+} ions on [B] sites, respectively.

The theoretical lattice parameter is shown in Table 1, which is found to match with the values calculated from the experimental details obtained through XRD.

The average crystallite size and density of $Zn_xNi_{1-x}Fe_2O_4$ nanoparticles are calculated using Debye Scherer formula [21–23] and are listed in Table 1. The doping of zinc in nickel ferrite enhances the grain growth and results in an increased crystallite size with respect to dopant concentration. The X-ray density $Zn_xNi_{1-x}Fe_2O_4$ nanoparticles decreases on addition of Zn in $Zn_xNi_{1-x}Fe_2O_4$ nanoparticles due to the variation in molecular weight and lattice parameter.

3.2. Morphological and compositional analysis of $Zn_xNi_{1-x}Fe_2O_4$ nanoparticles

The FE-SEM micrographs of PN0, PN2 and PN4 samples show the images of agglomerated nanoparticles (Fig. 3). The synthesized nanoparticles interact magnetically among each other which leads to the agglomeration.

PN0, PN2 and PN4 nanoparticles are found to be spherical with the average grain size in the range of 15–20 nm, 20–24 nm and 23–30 nm, respectively. Furthermore, TEM analysis has been done to further examine the particle size of nanoparticles with high resolution.

Fig. 4 shows the TEM micrographs and particle size distribution graphs of PN0, PN2 and PN4, which indicates that the synthesized nanoparticles are spherical in shape. The particle size of 17, 20 and 25 nm is observed for FN0, FN3 and FN4 samples, respectively, which is found to match well with the values obtained using Debye Scherer equation.

Table 2 shows the atomic percentage of all the elements in $Zn_xNi_{1-x}Fe_2O_4$ nanoparticles. The Zn peak gets more intense with the increase in dopant concentration as shown in Fig. 5.

Also, Zn/Ni ratio is increasing with respect to the dopant concentration and the values are found to match with the calculated ratio of x/(1-x) in $Zn_xNi_{1-x}Fe_2O_4$. These observations clearly substantiate the appropriate quantity of Zn doping in $NiFe_2O_4$ nanoparticles and proves the efficiency of synthesis.

3.3. Magnetic studies of $Zn_xNi_{1-x}Fe_2O_4$ nanoparticles

The $Zn_xNi_{1-x}Fe_2O_4$ nanoparticles exhibit nearly zero remanence and zero coercivity as shown in Fig. 6 suggesting the superparamagnetic behavior of synthesized nanoparticles. The critical size of $Zn_xNi_{1-x}Fe_2O_4$ nanoparticles for monodomain formation is found to be 40 nm,

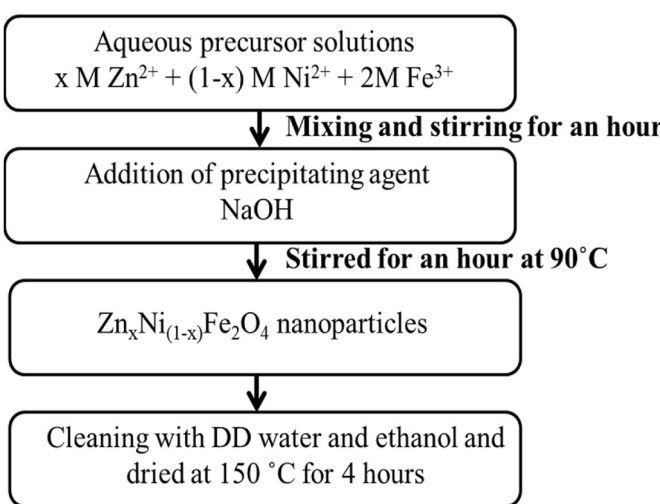


Fig. 1. Synthesis procedure of $Zn_xNi_{1-x}Fe_2O_4$ nanoparticles.

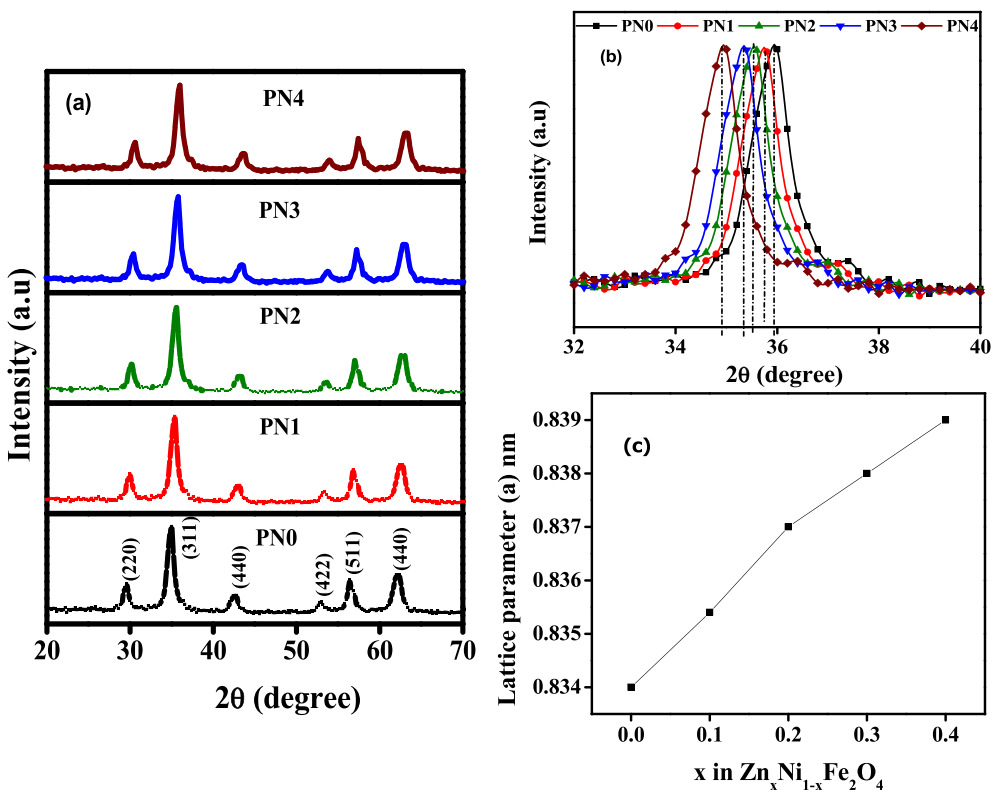


Fig. 2. (a) XRD patterns (b) Shift in (311) peak and (c) lattice parameter versus dopant concentration of $Zn_xNi_{(1-x)}Fe_2O_4$ nanoparticles.

Table 1
Crystallite size, lattice parameter and X-ray density of $Zn_xNi_{(1-x)}Fe_2O_4$ nanoparticles.

Sample	D (nm)	Lattice parameter (Å)		ρ_p (g/cm ³)
		a_{expt}	a_{th}	
PN0	16	8.34	8.33	5.367
PN1	18	8.35	8.34	5.363
PN2	21	8.37	8.37	5.339
PN3	23	8.38	8.38	5.335
PN4	24	8.39	8.40	5.331

which is comparable to the values reported by Iglesias et al. (2019) [24].

As the particle size of the synthesized $Zn_xNi_{(1-x)}Fe_2O_4$ nanoparticles is smaller than the critical size, the thermal energy is large enough to randomize the magnetic moments in the particle leading to zero net magnetization at zero field and favors superparamagnetism [1,25,26]. When the external field is applied, the magnetic moment of the atoms has a tendency to align in the magnetic field direction which leads to

higher magnetization.

The M – H curves of $Zn_xNi_{(1-x)}Fe_2O_4$ nanoparticles are fitted with the Langevin function [27,28] as shown in Fig. 7 and then log normal distribution (Fig. 8) is used to find the average particle size of the nanoparticles [29–31].

The magnetic particle diameters obtained from log-normal distribution are 16.5, 17.8, 20.2, 23.2 and 24.5 nm for FN0, FN1, FN2, FN3 and FN4, respectively. These values are found to match with those obtained from TEM micrographs as shown in Table 3.

The magnetization of $NiFe_2O_4$ nanoparticles is obtained as 19 emu/g which is higher than the value of 12 emu/g reported by Nabiyouni et al. (2010) and less than the bulk magnetization of 55 emu/g for the $NiFe_2O_4$ [2]. This is due to strong surface effect and reduced number of magnetic moments which are the consequences of reduced particle size.

From Table 4, it is observed that the saturation magnetization of $Zn_xNi_{(1-x)}Fe_2O_4$ nanoparticles enhances until the Zn concentration reaches $x = 0.2$ and decreases afterwards, which is similar to the observations reported by Hedao et al. [32]. In the undoped $NiFe_2O_4$ nanoparticles, equal number of Fe^{3+} ions occupy both the (A) and [B]

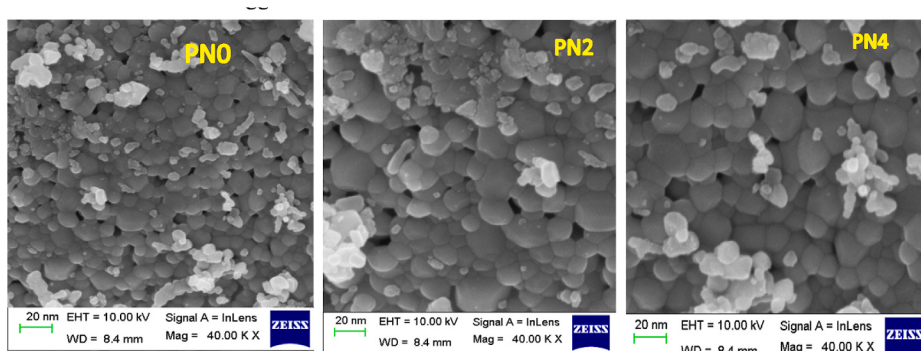


Fig. 3. FE-SEM micrographs of $Zn_xNi_{(1-x)}Fe_2O_4$ nanoparticles.

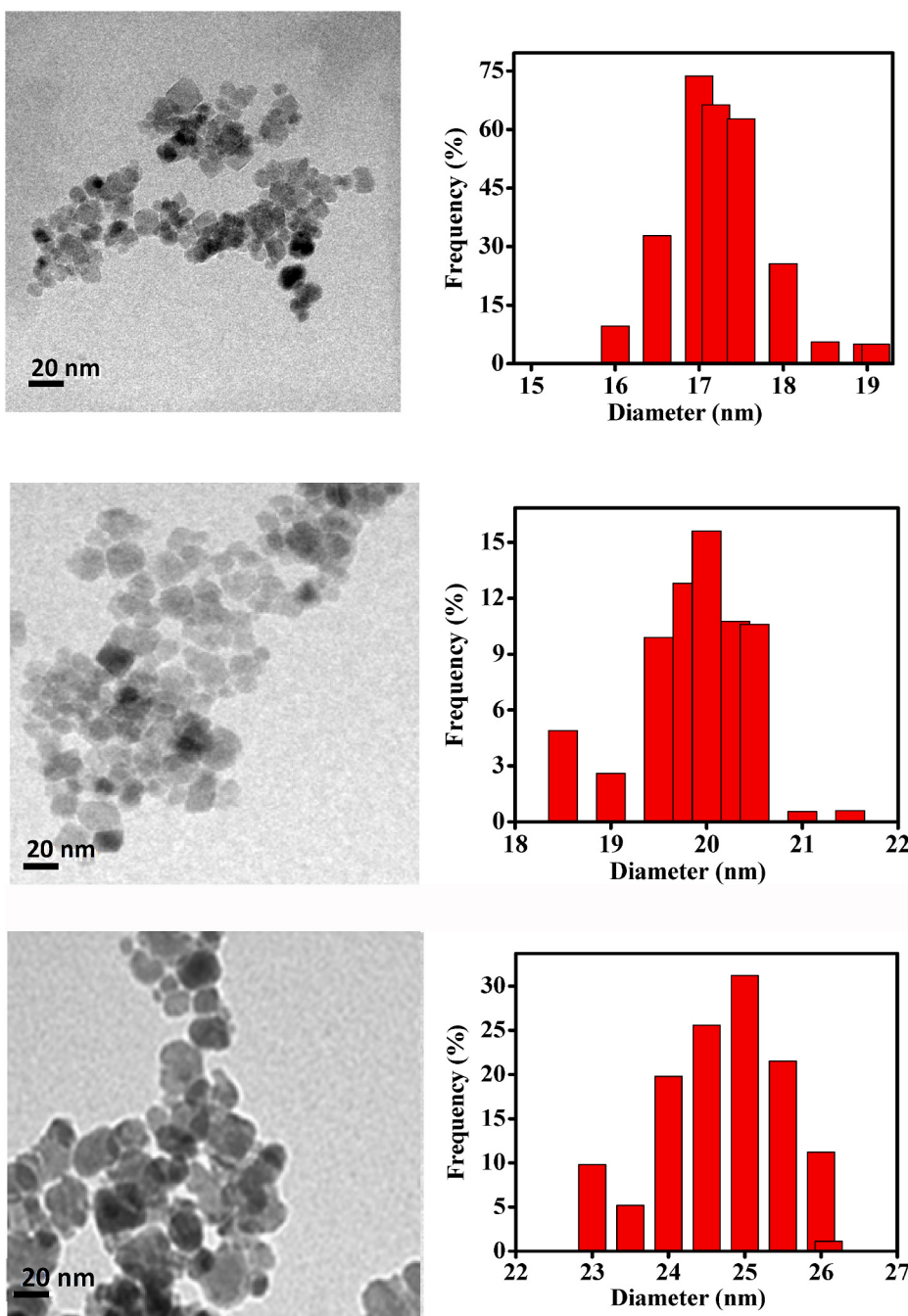


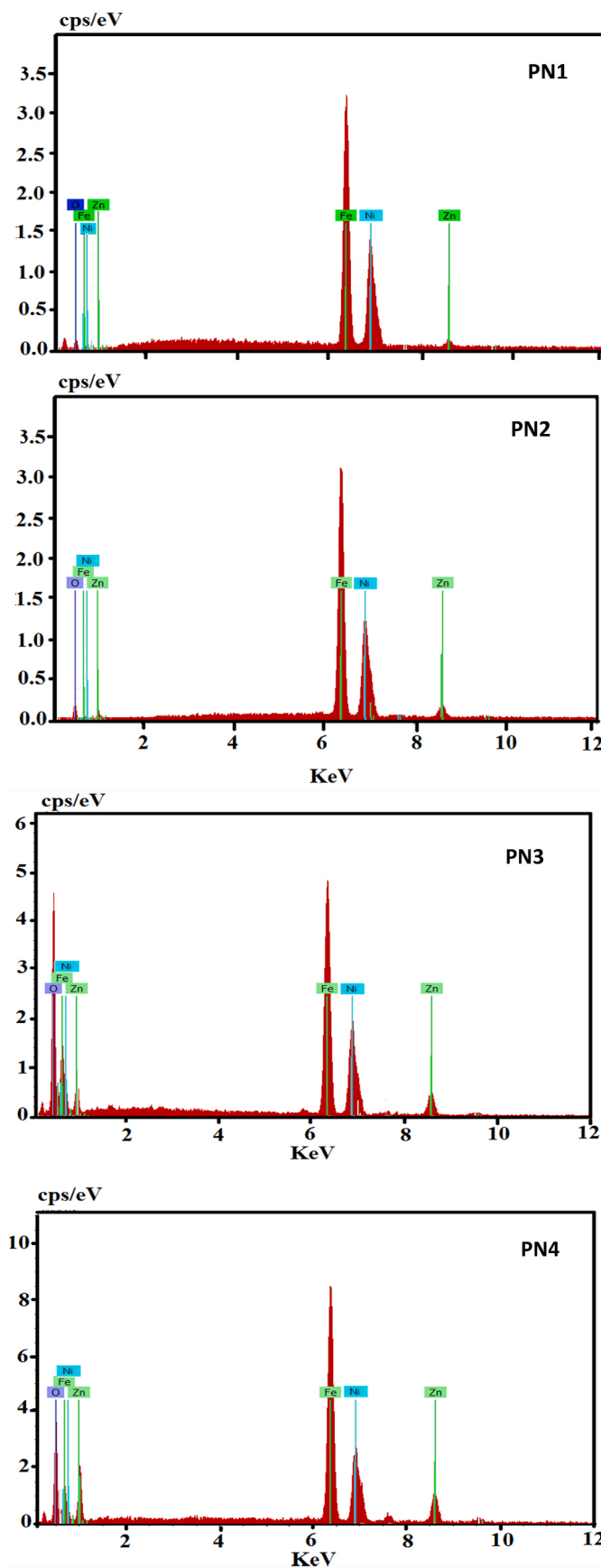
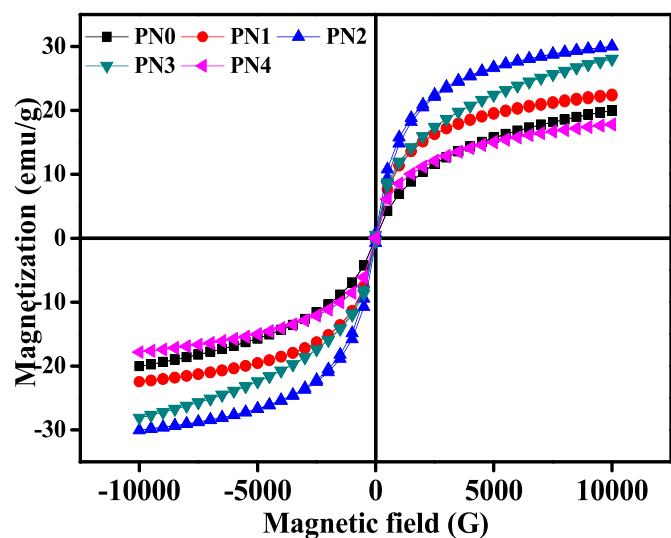
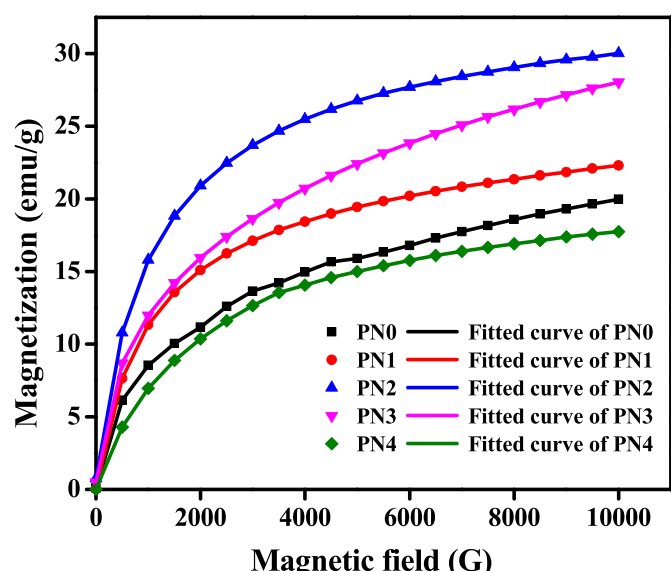
Fig. 4. TEM images and particle size distribution plots of (a) PN0 (b) PN1 and (c) PN4 particles.

Table 2
Atomic % of elements in $Zn_xNi_{(1-x)}Fe_2O_4$ nanoparticles.

Element	atomic %			
	PN1	PN2	PN3	PN4
Zn	1.29	3.10	4.21	5.80
Ni	12.91	12.41	9.80	8.67
Fe	28.4	31.02	28.02	28.94
O	57.4	53.47	57.97	56.59
Total	100	100	100	100
Zn/Ni	0.10	0.25	0.42	0.66
x/1-x	0.11	0.26	0.43	0.67

sites and are arranged in an antiparallel manner with respect to each other that leads to the cancellation of their magnetic moment. Hence, the overall magnetic moment is contributed by the Ni^{2+} ion in [B] site [5]. While doping, the Ni^{2+} ions are replaced with diamagnetic Zn^{2+} ions which have a preferential occupancy in (A) site of the cubic lattice that leads to the movement of same number of Fe^{3+} ions from (A) site to [B] site. This cationic distribution leads to an enhanced magnetization value until the dopant concentration reaches the critical value of $x = 0.2$. Above $x = 0.2$, the additional number of Zn^{2+} ion moves same number of Fe^{3+} ions from (A) site to [B] site but arranged in an antiparallel manner with respect to the neighbor ion due to the dominance of superexchange interaction than the double exchange interaction in [B] site [3,33]. Thus, the reduction in magnetization is observed in $Zn_xNi_{(1-x)}Fe_2O_4$ nanoparticles for $x > 0.2$.

Hence, the Zn concentration of $x = 0.2$ in $Zn_xNi_{(1-x)}Fe_2O_4$ is

Fig. 5. EDS Spectra of $Zn_xNi_{(1-x)}Fe_2O_4$ nanoparticles.Fig. 6. M – H plots of $Zn_xNi_{(1-x)}Fe_2O_4$ nanoparticles.Fig. 7. M – H plots of $Zn_xNi_{(1-x)}Fe_2O_4$ nanoparticles fitted with the Langevin function.

identified as a critical dopant concentration above which the bond angle of Fe–O–Ni reaches 180° that in turn contributes to the variation in exchange interactions and replicates as the above observed trend of magnetic properties.

3.4. Electrical conductivity studies on $Zn_xNi_{(1-x)}Fe_2O_4$ nanoparticles

A linear increase in current with an increasing voltage as shown in Fig. 9 (a) shows that the $Zn_xNi_{(1-x)}Fe_2O_4$ nanoparticles are Ohmic in nature. From the V-I measurements, the electrical resistance offered by $Zn_xNi_{(1-x)}Fe_2O_4$ nanoparticles is calculated and used for computing the electrical conductivity of $Zn_xNi_{(1-x)}Fe_2O_4$ nanoparticles. The electrical conductivity of undoped $NiFe_2O_4$ nanoparticles is found to be $10 \mu\text{S}/\text{cm}$, which is higher than the value of $3.2 \mu\text{S}/\text{cm}$ reported by Chandamma et al. (2017).

The electrical conduction in $Zn_xNi_{(1-x)}Fe_2O_4$ nanoparticles can be explained using Verway hopping mechanism [9]. According to that, the hopping of electrons and holes between same atoms of different valence states contributes to the electrical conduction in $Zn_xNi_{(1-x)}Fe_2O_4$.

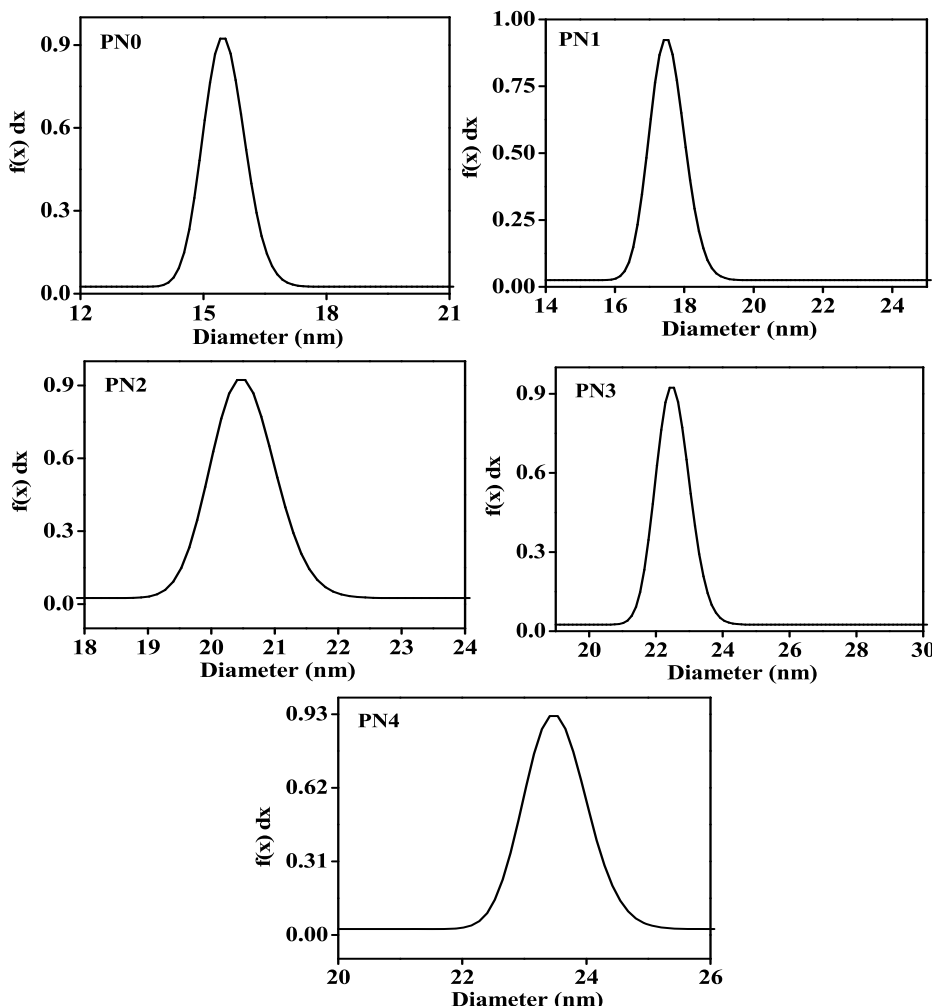


Fig. 8. Magnetic particle size distribution plots of $Zn_xNi_{(1-x)}Fe_2O_4$ nanoparticles obtained from Langevin function.

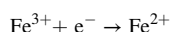
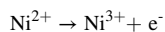
Table 3
Particle size comparison of $Zn_xNi_{(1-x)}Fe_2O_4$ nanoparticles.

Sample	Particle size (nm)	
	TEM	Langevin fitting
PN0	16.5	15.8
PN2	20.2	20.5
PN4	24.5	23.8

Table 4
Saturation magnetization of $Zn_xNi_{(1-x)}Fe_2O_4$ nanoparticles.

Sample	PN0	PN1	PN2	PN3	PN4
M_s (emu/g)	19	22	30	28	17

nanoparticles. The A-A and B-B site have higher hopping length than the A-B site of the spinel ferrites and hence, the hopping is highly possible in A-A and B-B site [34]. Among them, the hopping of ions are apparent in [B] site as it holds both the Ni^{2+} and Fe^{3+} ions instead of Fe^{3+} ions alone as in (A) site. The formation of Ni^{3+} and Fe^{2+} ions in [B] site for hopping is represented as below



The Ni^{2+} ion present in [B] site creates a hole vacancy by ejecting an

electron and results in the formation of Ni^{3+} ion. The Fe^{3+} ion takes up the ejected electron in the octahedral site and forms Fe^{2+} valance state. Now, the hopping takes place between the Fe^{3+} - Fe^{2+} and Ni^{2+} - Ni^{3+} ions in [B] sites which leads to an electrical conduction [34,35] in $Zn_xNi_{1-x}Fe_2O_4$ nanoparticles.

The inclusion of Zn enhances the electrical conductivity of $Zn_xNi_{1-x}Fe_2O_4$ nanoparticles up to the critical dopant concentration ($x = 0.2$) and decreases afterwards as shown in Fig. 9 (b). This is attributed to the increase in hopping probability of Fe^{3+} ions due to an increase in number of Fe^{3+} ions in the octahedral site of spinel ferrites on doping of Zn up to the critical concentration as discussed in section 3.3. Hence, the PN2 nanoparticles show higher conductivity of $41 \mu S/cm$, which is higher than the value reported by Chandamma et al. (2017). Further doping of Zn reduces the number of Fe^{3+} ions in octahedral site due to their antiparallel arrangement for maintaining the charge neutrality, which in turn affects the hopping probability and results in reduced electrical conductivity.

3.5. Surface charge studies on $Zn_xNi_{(1-x)}Fe_2O_4$ nanoparticles{write as in the heading}

The surface charge properties of $Zn_xNi_{(1-x)}Fe_2O_4$ nanoparticles are analyzed through the zeta potential values which are shown in Fig. 10.

Table 5 shows that the surface charge of $Zn_xNi_{(1-x)}Fe_2O_4$ nanoparticles is negative with an increasing trend up to the critical dopant concentration of $x = 0.2$, after which the surface charge declines. The electrons that contribute to nanoparticle conductivity contribute to the

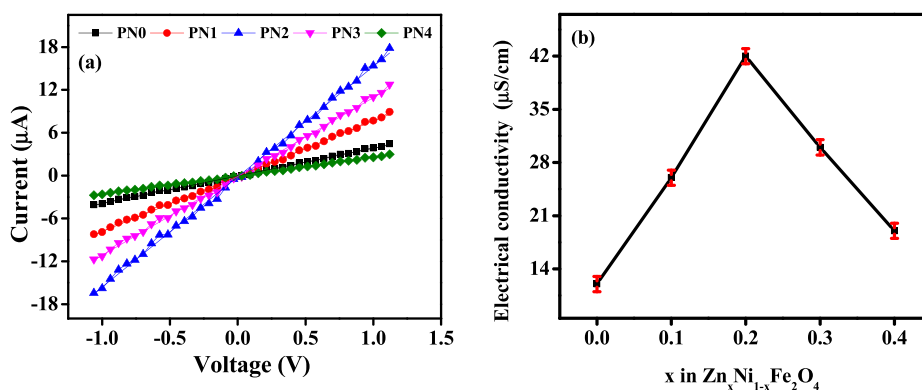


Fig. 9. a) I-V characteristics and b) Electrical conductivity versus dopant concentration plot of $Zn_xNi_{(1-x)}Fe_2O_4$ nanoparticles.

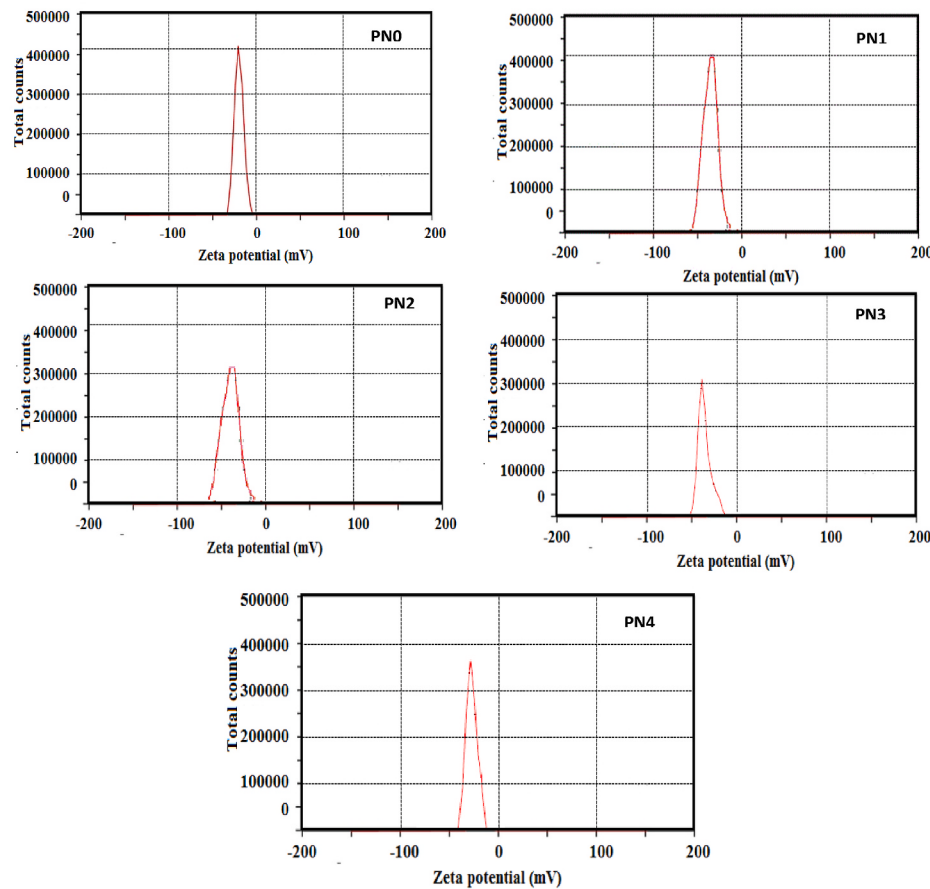


Fig. 10. Zeta potential distribution plots of $Zn_xNi_{(1-x)}Fe_2O_4$ nanoparticles.

Table 5
Zeta potential of $Zn_xNi_{(1-x)}Fe_2O_4$ nanoparticles.

Sample	PN0	PN1	PN2	PN3	PN4
Zeta potential (mV)	-20.5	-23.6	-29.7	-25.3	-22.4

surface charge also, thus leading to the similar trend as reported in Section 3.4. Because of the enhanced conductivity PN2 sample has the maximum zeta potential of -29.7 mV [34].

The above analyses show that the nanoparticles with critical dopant concentration of $x = 0.2$ in $Zn_xNi_{(1-x)}Fe_2O_4$ (PN2) nanoparticles shows enhanced magnetic, electrical and surface charge properties, due to

these desired characteristics they can be used in various biomedical applications.

4. Conclusion

The structural studies confirm the formation of phase pure face-centred cubic inverse spinel structure of $Zn_xNi_{(1-x)}Fe_2O_4$ nanoparticles. The appropriate amount of Zn doping in corresponding nanoparticles is confirmed using the EDX analysis. The morphological studies made through FE-SEM and TEM micrographs prove the spherical shape of the synthesized nanoparticles and also shows that the doping of Zn contributes to the variation in the particle size of $Zn_xNi_{(1-x)}Fe_2O_4$ nanoparticles. The superparamagnetic nature of the synthesized

nanoparticles is confirmed using the magnetic studies and the $Zn_{0.2}Ni_{0.8}Fe_2O_4$ nanoparticles shows the maximum magnetization of 30 emu/g. This is due to the domination of double exchange interaction over the superexchange interaction in the octahedral site of spinel ferrites with an inclusion of Zn dopant. Thus, $x = 0.2$ in the synthesized nanoparticles is identified as a critical dopant concentration, above which the bond angle of M-O-M reaches 180° , which in turn contributes to the variation in exchange interactions and results in the reduction in saturation magnetization. The M – H plots of the synthesized nanoparticles are fitted with the Langevin function to obtain the magnetic particle diameters and are found to match with the values obtained from TEM analysis. Similar to the observation of magnetization, the electrical conductivity and the surface charge of the synthesized nanoparticles increase with an inclusion of Zn until the value of $x = 0.2$, and then, a decreasing trend is noted. Verway hopping mechanism is used to explain the electrical conductivity of $Zn_xNi_{(1-x)}Fe_2O_4$ nanoparticles, according to which the conduction is due to the hopping of electrons between the Ni^{2+} and Fe^{3+} ions in the octahedral site of the spinel ferrite nanoparticles. The nanoparticles with critical dopant concentration exhibit higher values of electrical conductivity and surface charge due to the increased hopping probability as a consequence of higher number of Fe^{3+} ions in the octahedral site of $Zn_xNi_{(1-x)}Fe_2O_4$ nanoparticles. The synthesized nanoparticles have negative surface charge, and the maximum surface charge of -29.7 is exhibited by PN2 nanoparticles. Above the critical dopant concentration, the reduced number of Fe^{3+} ions in the octahedral site consequently reduces the electrical conduction and surface charge of the synthesized nanoparticles. These analyses prove that the synthesized nanoparticles with the critical dopant concentration of $x = 0.2$ is the best candidate which finds application in thermoelectrics, hyperthermia, magnetic coating and for the synthesis of conducting ferrofluids.

Declaration of competing interest

The authors declare that they have no known competing financial interests or personal relationships that could have appeared to influence the work reported in this paper.

References

- [1] D.V. Kurmude, C.M. Kale, P.S. Aghav, D.R. Shengule, K.M. Jadhav, Superparamagnetic behavior of zinc-substituted nickel ferrite nanoparticles and its effect on mossbauer and magnetic parameters, *J. Supercond. Nov. Magnetism* 27 (2014) 1889–1897, <https://doi.org/10.1007/s10948-014-2535-y>.
- [2] G. Nabiyouni, M.J. Fesharaki, M. Mozafari, J. Amighian, Characterization and Magnetic Properties of Nickel Ferrite Nanoparticles Prepared by Ball Milling Technique, vol. 27, 2010, pp. 6–9, <https://doi.org/10.1088/0256-307X/27/12/126401>.
- [3] B.H. Ong, E.S.C. Chee, S.B.O.A. Abd Hamid, K.P. Lim, Synthesis and characterization of nickel ferrite magnetic nanoparticles by co-precipitation method, *AIP Conf. Proc.* 1502 (2012) 221–229, <https://doi.org/10.1063/1.4769146>.
- [4] K. Maaz, S. Karim, A. Mumtaz, S.K. Hasanain, J. Liu, J.L. Duan, Synthesis and magnetic characterization of nickel ferrite nanoparticles prepared by co-precipitation route, *J. Magn. Magn Mater.* 321 (2009) 1838–1842, <https://doi.org/10.1016/j.jmmm.2008.11.098>.
- [5] N. Chandamma, B.M. Manohara, B.S. Ujjinappa, G.J. Shankarmurthy, M. V. Santhosh Kumar, Structural and electrical properties of Zinc doped Nickel ferrites nanoparticles prepared via facile combustion technique, *J. Alloys Compd.* 702 (2017) 479–488, <https://doi.org/10.1016/j.jallcom.2016.12.392>.
- [6] P. Deb, A. Basumallick, S. Das, Controlled synthesis of monodispersed superparamagnetic nickel ferrite nanoparticles, *Solid State Commun.* 142 (2007) 702–705, <https://doi.org/10.1016/j.ssc.2007.04.032>.
- [7] T. Anjaneyulu, A.T. Raghavender, K.V. Kumar, P.N. Murthy, K. Narendra, Influence of zinc doping in nickel ferrite nanoparticles synthesized by using an oxalic-acid-based precursor method, *J. Kor. Phys. Soc.* 62 (2013) 1114–1118, <https://doi.org/10.3938/jkps.62.1114>.
- [8] L.S. Sundar, K. Shusmita, M.K. Singh, A.C.M. Sousa, Electrical conductivity enhancement of nanodiamond-nickel (ND-Ni) nanocomposite based magnetic nanofluids, *Int. Commun. Heat Mass Tran.* 57 (2014) 1–7, <https://doi.org/10.1016/j.icheatmasstransfer.2014.07.003>.
- [9] B.H. Devmunde, A.V. Raut, S.D. Birajdar, S.J. Shukla, D.R. Shengule, K.M. Jadhav, Structural, electrical, dielectric, and magnetic properties of Cd 2+ substituted nickel ferrite nanoparticles, *J. Nanoparticles* 2016 (2016) 1–8, <https://doi.org/10.1155/2016/4709687>.
- [10] J.D. Arboleda, O. Arnache, M.H. Aguirre, R. Ramos, A. Anadón, M.R. Ibarra, Evidence of the spin Seebeck effect in Ni-Zn ferrites polycrystalline slabs, *Solid State Commun.* 270 (2018) 140–146, <https://doi.org/10.1016/j.ssc.2017.12.002>.
- [11] H. Ghayour, M. Abdellahi, N. Ozada, S. Jabbrzare, A. Khandan, SC, Elsevier Ltd, 2017, <https://doi.org/10.1016/j.jpcsc.2017.08.018>.
- [12] M. Sertkol, Y. Köse, A. Baykal, H. Kavas, A. Bozkurt, M.S. Toprak, Microwave Synthesis and Characterization of Zn-Doped Nickel Ferrite Nanoparticles, vol. 486, 2009, pp. 325–329, <https://doi.org/10.1016/j.jallcom.2009.06.128>.
- [13] A.B. Mugutkar, S.K. Gore, R.S. Mane, K.M. Batoo, S.F. Adil, S.S. Jadhav, Magneto-structural behaviour of Gd doped nanocrystalline Co-Zn ferrites governed by domain wall movement and spin rotations, *Ceram. Int.* 44 (2018) 21675–21683, <https://doi.org/10.1016/j.ceramint.2018.08.255>.
- [14] Y. Yang, H. Zhang, J. Li, Y. Rao, G. Wang, G. Gan, Bi3+ doping-adjusted microstructure, magnetic, and dielectric properties of nickel zinc ferrite ceramics for high frequency LTCC antennas, *Ceram. Int.* 46 (2020) 25697–25704, <https://doi.org/10.1016/j.ceramint.2020.07.046>.
- [15] H. Javed, F. Iqbal, P.O. Agboola, M.A. Khan, M.F. Warsi, I. Shakir, Structural, electrical and magnetic parameters evaluation of nanocrystalline rare earth Nd 3+-substituted nickel-zinc spinel ferrite particles, *Ceram. Int.* 45 (2019) 11125–11130, <https://doi.org/10.1016/j.ceramint.2019.02.176>.
- [16] T. Neuberger, B. Schöpf, H. Hofmann, M. Hofmann, B. Von Rechenberg, Superparamagnetic nanoparticles for biomedical applications: possibilities and limitations of a new drug delivery system, *J. Magn. Magn. Mater.* 293 (2005) 483–496, <https://doi.org/10.1016/j.jmmm.2005.01.064>.
- [17] M.A. Hakim, S.K. Nath, S.S. Sikder, K. Hanium Maria, Cation distribution and electromagnetic properties of spinel type Ni-Cd ferrites, *J. Phys. Chem. Solid.* 74 (2013) 1316–1321, <https://doi.org/10.1016/j.jpcs.2013.04.011>.
- [18] B.Y.R.D. Shannon, Revised effective ionic radii and systematic studies of interatomic distances in halides and chalcogenides, *Acta Crystallogr. A32* (1976) 751.
- [19] S.A. Mazen, M.H. Abdallah, R.I. Nakhla, H.M. Zaki, F. Metawe, X-ray analysis and IR absorption spectra of Li-Ge ferrite, *Mater. Chem. Phys.* 34 (1993) 35–40, [https://doi.org/10.1016/0254-0584\(93\)90116-4](https://doi.org/10.1016/0254-0584(93)90116-4).
- [20] R. Das, S. Sarkar, Determination of intrinsic strain in poly(vinylpyrrolidone)-capped silver nano-hexapod using X-ray diffraction technique, *Curr. Sci. 109* (2015) 775–778, <https://doi.org/10.18520/cs/v109/i4/775-778>.
- [21] S. Mirzaee, Y. Azizian-Kalandaragh, P. Rahimzadeh, Modified co-precipitation process effects on the structural and magnetic properties of Mn-doped nickel ferrite nanoparticles, *Solid State Sci.* 99 (2020) 106052, <https://doi.org/10.1016/j.solidstatesciences.2019.106052>.
- [22] M. Shoaib-Ur-Rehman, Z. Javaid, I. Asghar, M. Azam, S. Shukrullah, F. Iqbal, A. Maqsood, M.Y. Naz, Photo-catalytic response of zinc-doped nickel ferrite nanoparticles for removal of chromium from industrial wastewater, *IOP Conf. Ser. Mater. Sci. Eng.* 863 (2020), <https://doi.org/10.1088/1757-899X/863/1/012017>.
- [23] P. Aakash, Nordblad, Rajendra Mohan, S. Mukherjee, Structural, magnetic and hyperfine characterizations of nanocrystalline Zn-Cd doped nickel ferrites, *J. Magn. Magn Mater.* 441 (2017) 710–717, <https://doi.org/10.1016/j.jmmm.2017.06.040>.
- [24] S.P. Iglesias, A. Arias-Durán, J.M. Yañez-Limón, R. Ramirez-Bon, A. Hurtado-Macias, O. Arnache, M.E. Gómez, W. Lopera, G. Zambrano, Effect of Zn concentration on the structure, morphology, and magnetic behavior of $Ni_1 - xZn_xFe_2O_4$ ferrofluid, *J. Supercond. Nov. Magnetism* 32 (2019) 2199–2208, <https://doi.org/10.1007/s10948-018-4950-y>.
- [25] A.M.A. Henaish, M.M. Ali, D.E.E. Refaay, I.A. Weinstein, O.M. Hemeda, Synthesis, electric and magnetic characterization of nickel ferrite/PANI nano-composite prepared by flash auto combustion method, *J. Inorg. Organomet. Polym. Mater.* 31 (2021) 731–740, <https://doi.org/10.1007/s10904-020-01737-w>.
- [26] M. Nabeel Rashin, J. Hemalatha, Magnetic and ultrasonic investigations on magnetite nanofluids, *Ultrasonics* 52 (2012) 1024–1029, <https://doi.org/10.1016/j.ultras.2012.08.005>.
- [27] K. Anu, J. Hemalatha, Magnetic and electrical conductivity studies of zinc doped cobalt ferrite nanofluids, *J. Mol. Liq.* 284 (2019) 445–453, <https://doi.org/10.1016/j.molliq.2019.04.018>.
- [28] K. Anu, J. Hemalatha, Ultrasonic and magnetic investigations of the molecular interactions in zinc doped magnetite Nanofluids, *J. Mol. Liq.* 256 (2018) 213–223, <https://doi.org/10.1016/j.molliq.2018.02.037>.
- [29] M. Raşa, Magnetic properties and magneto-birefringence of magnetic fluids, *Eur. Phys. J. E.* 2 (2000) 265–275, <https://doi.org/10.1007/PL00013670>.
- [30] D.X. Chen, A. Sanchez, E. Taboada, A. Roig, N. Sun, H.C. Gu, Size determination of superparamagnetic nanoparticles from magnetization curve, *J. Appl. Phys.* 105 (2009), <https://doi.org/10.1063/1.3117512>.
- [31] A. Józefczak, B. Leszczyński, A. Skumię, T. Horowski, A comparison between acoustic properties and heat effects in biogenic (magnetosomes) and abiotic magnetite nanoparticle suspensions, *J. Magn. Magn Mater.* 407 (2016) 92–100, <https://doi.org/10.1016/j.jmmm.2016.01.054>.
- [32] P.S. Hedao, D.S. Badwaik, S.M. Suryawanshi, K.G. Rewatkar, Structural and magnetic studies of Zn doped nickel nanoferrites synthesize by sol-gel auto combustion method, *Mater. Today Proc.* 15 (2019) 416–423, <https://doi.org/10.1016/j.matpr.2019.04.102>.

- [33] S.S. Pati, J. Philip, A facile approach to enhance the high temperature stability of magnetite nanoparticles with improved magnetic property, *J. Appl. Phys.* 113 (2013), <https://doi.org/10.1063/1.4789610>.
- [34] R.S. Barkule, D.V. Kurmude, A.V. Raut, N.N. Waghule, K.M. Jadhav, D.R. Shengule, Structural and electrical conductivity studies in nickel ferrite nanoparticles, *Solid State Phenom.* 209 (2014) 177–181. <https://doi.org/10.4028/www.scientific.net/SSP.209.177>.
- [35] G. Srinivasan, C.M. Srivastava, Electrical conductivity mechanism in zinc and copper substituted magnetite, *Phys. Status Solidi* 103 (1981) 665–671, <https://doi.org/10.1002/pssb.2221030226>.